Journal of *Marine Science and Engineering*

MDPI

Article

Mission Effectiveness Assessment of Solar-Powered Unmanned Surface Vehicles Considering Hardware States and Energy Levels

Yaqiang Lu, Jipeng Zhang, Chao Song, Fankai Meng * and Yu Song *

School of Power Engineering, Naval University of Engineering, Wuhan 430033, China; m25180705@nue.edu.cn (Y.L.); m24180702@nue.edu.cn (J.Z.); m24380701@nue.edu.cn (C.S.)
* Correspondence: 1208061076@nue.edu.cn (F.M.); 2020201030@nue.edu.cn (Y.S.)

Abstract

An improved availability–dependability–capability (ADC) assessment framework is proposed for evaluating the mission effectiveness of solar-powered unmanned surface vehicles (USVs) under the coupled effects of hardware state transitions and stochastic energy supply. Within the availability and dependability dimensions, a joint state space is constructed that couples hardware condition states with battery state of charge (SOC). A Monte Carlo simulation driven by real solar irradiance data is used to derive the initial probability distribution and the dynamic state transition matrix. In the capability dimension, a hierarchical index system is established, and a hierarchical Criteria Importance Through Intercriteria Correlation (CRITIC) method is introduced to achieve objective weighting that accounts for inter-index correlations across multiple levels. Case-study calculations for a typical task profile yield a baseline mission effectiveness of approximately 0.661934. Comparative analysis reveals that neglecting the dynamic evolution of the energy state overestimates effectiveness by 38.94%, whereas ignoring random hardware failures produces a deviation of roughly 9.48%. These findings indicate that, while energy-state dynamics impose the dominant constraint on mission performance, the contribution of hardware degradation remains substantial. The concurrent influence of both limiting factors confirms the necessity of an assessment framework that explicitly integrates hardware and energy states, as developed in this work.

Keywords: availability–dependability–capability (ADC) model; Monte Carlo simulation; CRITIC method; solar-powered unmanned surface vehicle

1. Introduction

Solar-powered unmanned surface vehicles (USVs) harness renewable energy and offer long-endurance autonomous operation, positioning them as increasingly important maritime intelligent platforms. Equipped with diverse mission payloads, they hold considerable promise for applications such as ocean environmental monitoring and wide-area reconnaissance [1,2]. Accurate assessment of their mission effectiveness is essential for equipment demonstration, mission planning, and performance optimization.

The availability–dependability–capability (ADC) model, proposed by the Weapon System Effectiveness Industry Advisory Committee, has been widely adopted in unmanned system effectiveness evaluation owing to its conceptual clarity and rigorous structure [3]. However, the model reduces the system state to a binary operational/failed representation and relies on a subjectively assigned capability vector. As a result, it cannot objectively capture real-world effectiveness under multi-factor coupling [4]. This limitation is particularly

Check for updates

Received: 7 June 2026
Revised: 26 June 2026
Accepted: 29 June 2026
Published: 30 June 2026

Copyright: © 2026 by the authors. Licensee MDPI, Basel, Switzerland. This article is an open access article distributed under the terms and conditions of the Creative Commons Attribution (CC BY) license.

critical for solar-powered unmanned surface vehicles (USVs). The effectiveness of these platforms depends strongly on intermittent solar input and on system states that evolve dynamically over the mission course in response to complex ocean environments.

Previous efforts to construct the availability vector have focused on the effectiveness evaluation of marine unmanned aerial vehicles (UAVs), conventional UAVs, and underwater gliders. These studies typically characterize the system state as binary (operational or failed) and derive the initial state probability directly from static reliability data. This approach has established a practical foundation for effectiveness analysis [5–7]. Despite this progress, the binary state representation inherently overlooks the impact of real-time energy reserve on mission readiness. Discrete energy state modelling has demonstrated clear advantages in fault-tolerant UAV mission management and multi-battery energy system reconfiguration [8,9]. In these contexts, it captures the influence of energy dynamics on mission capability. Its application in the effectiveness evaluation of energy-dependent unmanned marine systems, however, remains unexplored. To address this gap, the present work introduces an availability vector that simultaneously accounts for hardware state and battery state of charge (SOC). Energy level is discretised according to solar energy replenishment and mission power consumption, so that the initial state probability reflects both the failure rate and the actual energy state.

Previous efforts to construct the capability vector have focused on aggregating multi-dimensional performance indicators through subjective weighting methods. These studies commonly adopt the Analytic Hierarchy Process (AHP) to synthesize diverse performance metrics. Bi et al. [10], for instance, integrated AHP with interval-valued evidential reasoning to develop a weapon system effectiveness assessment method, establishing a practical decision-making framework. Despite the utility of such expert-driven approaches, their reliance on subjective judgement limits objectivity and reproducibility, particularly when indicators exhibit substantial information overlap and conflict. The CRITIC (Criteria Importance Through Intercriteria Correlation) method has demonstrated clear advantages in handling inter-criteria correlations in reservoir evaluation, ship risk assessment [11,12], and marine diesel engine optimization [13,14]. In these applications, it objectively resolves conflicting multi-criteria interactions to produce reproducible, data-driven evaluations. Its application in the effectiveness modelling of energy-dependent unmanned systems, however, remains unexplored. To address this gap, the present work introduces a hierarchical CRITIC-based weighting scheme for the capability dimension of the ADC framework. Indicator weights are derived from the contrast intensity and conflict measured across criteria, yielding a fully data-driven capability vector that eliminates subjective assignment.

By integrating these two modelling advances, this study develops an improved ADC effectiveness assessment framework that explicitly captures the coupled dynamics of hardware condition states and stochastic solar energy supply. The principal contributions are summarized as follows:

- **A joint state-space modelling approach:** The traditional binary "normal/failed" assumption is replaced by a hardware–energy joint state space in both the Availability and Dependability dimensions. This enables the initial availability vector and dynamic state transition matrix to be solved via a Monte Carlo simulation driven by real solar irradiance data, thereby eliminating the artificial assumption of a static initial battery state.

- **Objective capability weighting:** A hierarchical mission capability index system is established, and a hierarchical CRITIC method is introduced to achieve objective weighting. This scheme resolves multi-criteria conflicts among capability indicators while eliminating the subjectivity inherent in traditional empirical or expert-based assignment methods.
- **Quantitative isolation of dynamic coupling effects:** Through comparative scenario analysis, the independent impacts of energy-state dynamics and random hardware failures on mission effectiveness are quantitatively decoupled, providing direct numerical evidence for the relative contribution of each limiting factor. The results quantitatively demonstrate that dynamic energy attenuation is the dominant performance constraint for this class of energy-dependent unmanned marine platforms, yet the contribution of hardware degradation remains substantial. Taken together, these results confirm that both limiting factors must be explicitly integrated within the assessment framework.

The remainder of this paper is organized as follows. Section 2 details the basic principle of the ADC model and its specific improvements. Section 3 elaborates the entire process of mission effectiveness modelling, including state-space construction, Monte Carlo solution, and hierarchical CRITIC weighting. Section 4 presents a case study with simulation results and comparative analysis. Section 5 discusses the implications, limitations, and conclusions of this work.

2. ADC Model and Its Improvement

2.1. Basic Principle of the ADC Model

The ADC model expresses system effectiveness as the product of the availability vector **A**, the dependability matrix **D**, and the capability vector **C**:

$$E = \mathbf{A} \cdot \mathbf{D} \cdot \mathbf{C} \tag{1}$$

The model decomposes effectiveness E into three elements: the initial availability probability **A** at the start of a mission, the state dependability **D** during the mission, and the capability **C** to accomplish the mission objective in each state.

For long-endurance solar-powered USVs, mission effectiveness depends critically on both intermittent solar energy supply and system state evolution in complex ocean environments. Conventional methods cannot capture the dynamic interactions between energy availability and system state, nor can they construct an objective and accurate capability matrix. To address these limitations, this study adapts the ADC model to build an assessment framework that explicitly couples hardware condition states with stochastic energy supply.

2.2. Improved ADC Model

2.2.1. Improvement of the Availability Vector

The conventional availability vector accounts solely for hardware states. Suppose the system can reside in n discrete hardware states; the availability vector is then expressed as $\mathbf{A}_{\text{free}} = [a_1, a_2, \ldots, a_n]$, where a_i denotes the probability that the system is in state i at the start of a mission [15]. The improved availability vector simultaneously considers the hardware state and the initial energy level. Let the number of hardware states be n_h, with the state set $\mathcal{H} = 1, 2, \ldots, n_h$. The battery state of charge (SOC) is discretized into n_e levels, with the state set $\mathcal{E} = 1, 2, \ldots, n_e$. The joint state space is defined as $S = \mathcal{H} \times \mathcal{E}$, and the total number of states is

$$N = n_h \cdot n_e \tag{2}$$

The improved availability vector $\mathbf{A}$ is then given by $\mathbf{A} = (a_{1,1}, a_{1,2}, \ldots, a_{n_h,n_e})_{1\times N}$, where $a_{i,j}$ is the probability that the system is in hardware state i and SOC level j at the mission start.

2.2.2. Reconstruction of the Dependability Matrix

The dependability matrix $\mathbf{D}$ describes the probabilities of the system transitioning from initial states to other states during mission execution, and its dimensions must be consistent with the state space of the availability vector $\mathbf{A}$ [16]. Since the availability vector has been extended from a single hardware state to a hardware–energy joint state, the dependability matrix must correspondingly be expanded from an n-order matrix that describes only hardware failure transitions to an N-order matrix describing joint state transitions:

$$\mathbf{D} = [d_{s\to s'}]_{N\times N} \tag{3}$$

2.2.3. Improvement of the Capability Vector

The capability vector $\mathbf{C}$ represents the inherent ability of the system to accomplish its mission in each hardware state. For a solar-powered USV, mission capability degrades continuously with the battery SOC and requires a multidimensional comprehensive evaluation; consequently, a constant value assignment and subjective empirical weighting are no longer applicable. The capability vector is reconstructed as follows: dimensionally, $\mathbf{C}$ is extended from n to N dimensions to match the joint state space; in terms of assignment logic, the capability value of each state is differentiated according to the energy level; and for weighting, objective weighting principles are introduced to replace traditional subjective methods. Detailed modelling and weighting procedures are presented in Section 3.3.

The core modelling assumptions of the improved ADC framework are summarized below, together with their rationales and principal limitations. First, the hardware system is represented by a binary operational/failed state set, with failures treated as irreparable within a single mission; this simplification is consistent with practical engineering scenarios, because typical mission durations are substantially shorter than the mean time to repair, and both the MTBF and MTTR parameters fall within the ranges widely adopted in reliability studies of small marine unmanned platforms. Second, constant base and mission load profiles are used so that the analysis focuses on the coupling between hardware state transitions and energy evolution rather than on dynamic power fluctuations induced by variable sea states. Third, the continuous battery SOC is discretised into five equal intervals, balancing state characterization accuracy against computational efficiency. Fourth, Gaussian random noise with a relative standard deviation of 5% is superimposed on typical meteorological year hourly irradiance data to capture short-term solar fluctuations in coastal waters. These simplifications are introduced to ensure analytical tractability and to keep the study focused on the core coupling mechanism between hardware health and energy status; at the same time, they define the applicable boundaries of the current model. The binary hardware abstraction does not capture graded component degradation or degraded operation under partial faults. The fixed-load assumption may deviate from actual dynamic power consumption under high sea states. The discretised SOC scheme introduces inherent quantisation error and cannot resolve fine-grained state evolution. The Gaussian noise formulation cannot fully represent abrupt irradiance variations caused by extreme weather events. These boundaries are inherent to the modelling strategy adopted here and point to directions for further refinement in future work.

3. Effectiveness Modelling and Evaluation of Solar-Powered USVs

3.1. Joint State Space Construction and Availability Modelling

3.1.1. Joint State Space Construction

The initial state of a solar-powered USV before a mission is jointly determined by hardware state and battery SOC. The hardware state is classified into two categories: operational (H_1) and failed (H_2). Their probabilities are determined by the mean time between failures (MTBF) and the mean time to repair (MTTR):

$$\begin{aligned} P(H_1) &= \frac{MTBF}{MTBF+MTTR} \\ P(H_2) &= \frac{MTTR}{MTBF+MTTR} \end{aligned} \tag{4}$$

The battery SOC ranges from 0 to 1. Introduce $(n_e - 1)$ thresholds such that $0 = \theta_0 < \theta_1 < \cdots < \theta_{n_e-1} < \theta_{n_e} = 1$; the j-th energy level E_j corresponds to SOC $\in [\theta_{j-1}, \theta_j)$, $j = 1, 2, \ldots, n_e$. Here we set $n_e = 5$ with thresholds $\theta_0 = 0, \theta_1 = 0.2$, $\theta_2 = 0.4$, $\theta_3 = 0.6$, $\theta_4 = 0.8$, $\theta_5 = 1$. Thus the energy levels from high to low are: E_1 [0.8, 1], E_2 [0.6, 0.8), E_3 [0.4, 0.6), E_4 [0.2, 0.4), E_5 [0, 0.2). The joint state space comprises 10 states, ordered by hardware priority: the first five states are hardware-normal with descending energy levels, $X_1 = (H_1, E_1), X_2 = (H_1, E_2), \ldots, X_5 = (H_1, E_5)$; the last five are hardware-failed with descending energy levels, $X_6 = (H_2, E_1), \ldots, X_{10} = (H_2, E_5)$.

3.1.2. Monte Carlo Simulation for the Initial Probability Distribution

Before receiving a mission, the USV may undergo a stochastic standby or pre-deployment period during which hardware failures and repairs can occur, and the initial SOC becomes random owing to fluctuating solar irradiance. A Monte Carlo simulation procedure is therefore adopted to derive the initial joint state probability distribution [17–20].

The overall Monte Carlo framework is illustrated in Figure 1. First, system parameters are set, including battery rated capacity E_{bat}, charging/discharging efficiencies η_{ch} and η_{dis}, SOC limits SOC_{min} and SOC_{max}, standby power load P_{standby}, maximum charge/discharge powers P_{chmax} and P_{dismax}, hardware reliability parameters MTBF/MTTR, and total simulation duration T_h. Typical meteorological year (TMY) hourly irradiance data are loaded and perturbed with random noise: $I_{\text{perturbed}}(\text{t}) = I_{\text{TMY}}(\text{t}) \cdot [1 + \epsilon(\text{t})]$ with $\epsilon(t) \sim \mathcal{N}(0, 0.05^2)$, then converted to photovoltaic (PV) power generation $P_{\text{pv}}(t)$ via a PV model [21,22]. With the total number of simulation runs set to N_{mc}, each run executes the hardware state simulation submodule(which generates failure state arrays) and the energy management submodule (which updates the SOC stepwise); the final SOC and hardware state after a warm-up period are recorded [23,24]. After all runs, the frequencies f_s of each joint state are tallied and normalized to obtain the initial probability, i.e., the initial availability vector **A**.

The hardware state simulation submodule (Figure 2) initializes the current time and system state as "normal." If the current state is normal, a time-to-failure $T_f \sim \exp(1/\text{MTBF})$ is generated; the failure onset time $t_f = t + T_f$ is computed. If $t_f < T_h$, the normal state persists until t_f and then transitions to the failed state; otherwise, normal operation continues until T_h. If the current state is failed, a repair time $T_r \sim \exp(1/\text{MTTR})$ is generated; the repair completion time $t_r = t_f + T_r$ is calculated. If $t_r < T_h$, the failed state lasts until t_r and then reverts to normal, updating the current time to the next discrete step; otherwise, the failed state persists until T_h. The output is a hardware state sequence at each discrete time step.

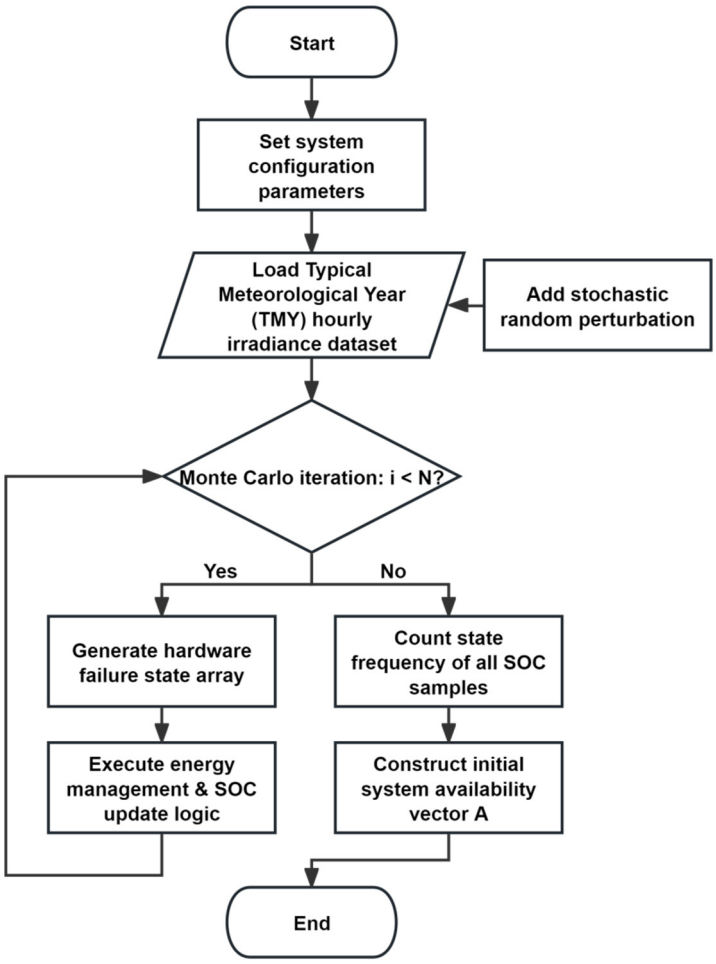


Figure 1. Flowchart of the overall Monte Carlo simulation framework.

The energy management submodule operates as follows. The system collects real-time PV output power and load consumption power, and determines the battery charging/discharging mode according to the power difference.

When $P_{\mathrm{pv}} > P_{\mathrm{load}}$, the system enters the charging mode, and the surplus power charges the battery under the constraints:

$$\text{s.t.}\begin{cases} \Delta E = \left(P_{\mathrm{pv}} - P_{\mathrm{load}}\right) \times \Delta t \\ E_t = \Delta E \times \eta_{\mathrm{ch}} \\ E_{\mathrm{remaining}} = \left(SOC_{\max} - SOC\right) \times E_{bat} \\ E_{\mathrm{charge}} = \min\left(E_t,\ E_{\mathrm{remaining}},\ P_{\mathrm{chmax}} \times \Delta t\right), \\ SOC_{\mathrm{new}} = SOC + \frac{E_{\mathrm{charge}}}{E_{\mathrm{bat}}} \end{cases} \tag{5}$$

where ΔE is the surplus energy in the simulation step Δt, E_r is the theoretical chargeable energy accounting for efficiency, $E_{\mathrm{remaining}}$ is the remaining capacity the battery can accept, and E_{charge} is the actual charged energy subject to the three upper bounds; the SOC is then updated.

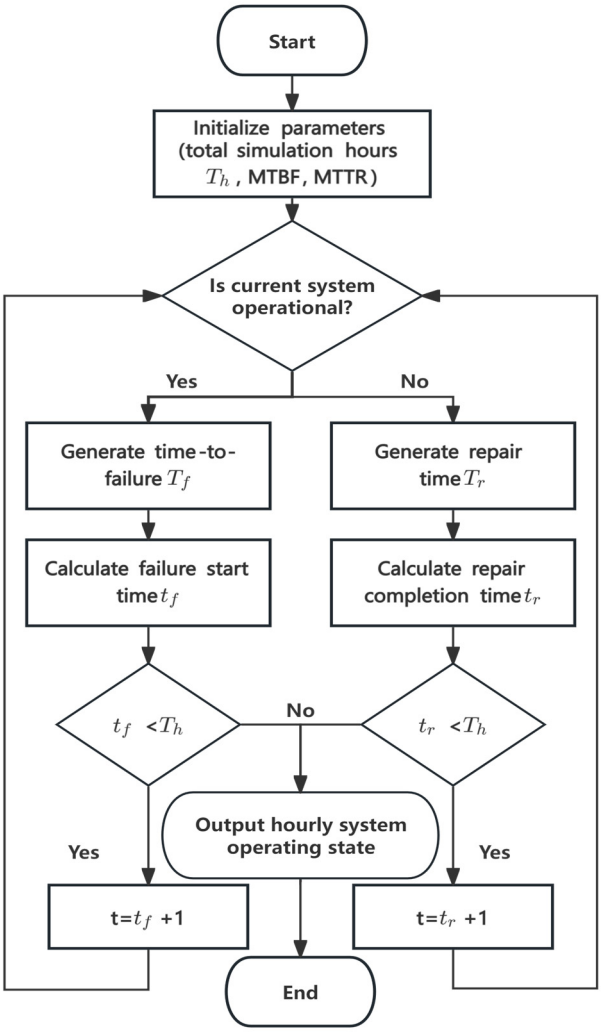


Figure 2. Flowchart of the hardware state simulation submodule.

When $P_{\text{pv}} \leq P_{\text{load}}$, the PV output cannot meet the load demand, and the system switches to discharging mode:

$$\text{s.t.} \begin{cases} \Delta E = \left(P_{\text{load}} - P_{\text{pv}}\right) \times \Delta t \\ E_f = \frac{\Delta E}{\eta_{\text{dis}}} \\ E_{\text{available}} = \left(SOC - SOC_{\text{min}}\right) \times E_{bat} \\ E_{\text{discharge}} = \min\left(E_f,\ E_{\text{available}},\ P_{\text{dismax}} \times \Delta t\right) \\ SOC_{\text{new}} = SOC - \frac{E_{\text{discharge}}}{E_{\text{bat}}} \end{cases}, \tag{6}$$

where ΔE is the energy deficit, E_f is the theoretical required discharge energy after efficiency, $E_{\text{available}}$ is the available capacity, and $E_{\text{discharge}}$ is the actual discharged energy constrained by the three lower bounds; the SOC is then updated [25,26].

3.2. Dynamic Dependability Modelling and Transition Probability Solution

3.2.1. State Transition Process Analysis

System state transitions arise from the coupled evolution of stored energy and random changes in hardware condition. The hardware state alternates stochastically between normal and failed conditions: upon failure, the load is degraded and photovoltaic generation is suspended. A critically low SOC triggers protective shutdown. The resulting one-step transition probability matrix D exhibits a strictly upper-block-triangular structure:

$$D = \begin{bmatrix} \mathrm{D_{HH}} & \mathrm{D_{HF}} \\ 0 & \mathrm{D_{FF}} \end{bmatrix} \tag{7}$$

The subscript H denotes hardware-normal states and F hardware-failed states. The submatrix $\mathbf{D}_{HH}$ captures the internal evolution among energy levels under normal hardware conditions; $\mathbf{D}_{HF}$ represents the one-way transition channel from normal to failed states; and $\mathbf{D}_{FF}$ describes energy-level migration under failed hardware. The zero block in the lower-left corner reflects the physical constraint that, within a single mission, a hardware failure is irreparable and the system cannot return to a normal state; it can evolve only within the failure-state group.

3.2.2. Monte Carlo Solution of the Transition Probability Matrix

Using the mission duration T_{mission} as the simulation horizon and the availability vector $\mathbf{A}$ as the initial distribution for sampling, transition frequencies from each initial state s to each final state s' are tallied to obtain the transition probability:

$$\mathrm{d_{s\to s'}(T_{mission})} = \frac{\mathrm{n_{s\to s'}(T_{mission})}}{\sum_{s'} \mathrm{n_{s\to s'}(T_{mission})}} \tag{8}$$

3.3. Capability Modelling and Hierarchical CRITIC Weighting

3.3.1. Index System Construction

Based on the typical mission requirements of a solar-powered USV, a hierarchical mission capability index system is established, as illustrated in Figure 3 [27,28]. Five second-level capability indicators ($m = 5$) are defined: maneuvering capability, detection and identification capability, on-site evidence acquisition capability, communication and data transmission capability, and autonomous reconnaissance and collaboration capability. Each second-level indicator comprises several quantifiable third-level indicators, totaling $p = 19$.

For any joint state X_s, the comprehensive capability value is the linear weighted sum of the dimensionless scores of the second-level indicators:

$$c_s = \sum_{k=1}^{m} \lambda_k \cdot P_k^{(s)}, \tag{9}$$

where λ_k is the weight of the k-th second-level indicator, and $P_k^{(s)}$ is its dimensionless normalized score in state s (range [0, 1]).

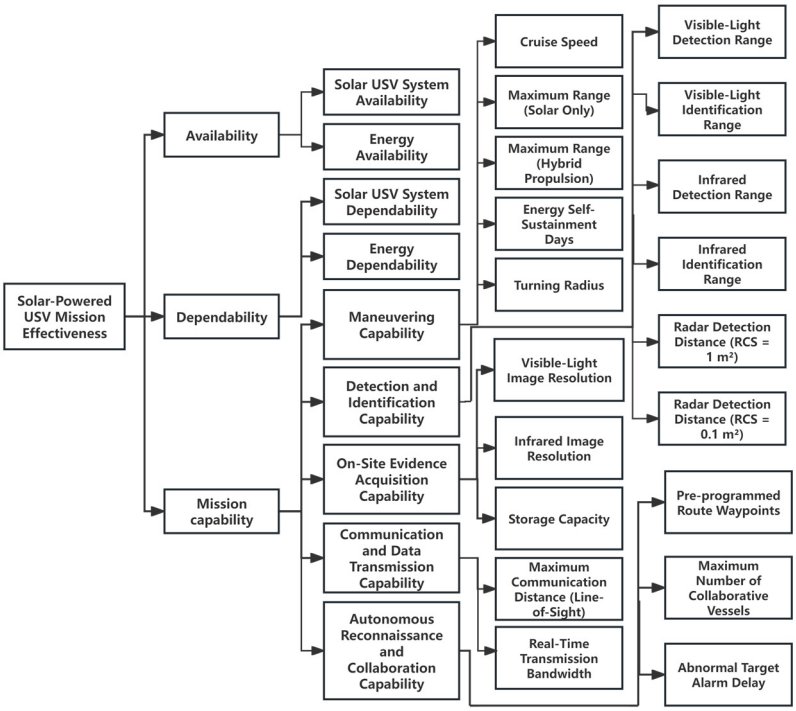


Figure 3. Mission effectiveness evaluation index system of the solar-powered USV.

The dimensionless value of a second-level indicator is synthesized from its subordinate third-level indicators:

$$P_k^{(s)} = \sum_{v \in \Omega_k} \omega_v \cdot y_{sv}, \tag{10}$$

where Ω_k is the set of third-level indicators under the k-th second-level indicator, ω_v is the local weight of the third-level indicator, and y_{sv} is its standardized value.

The overall capability can be expressed directly using global weights:

$$c_s = \sum_{v=1}^{p} w_v^{(\text{global})} \cdot y_{sv}, \tag{11}$$

where $w_v^{(\text{global})}$ is the global weight of the third-level indicator, obtained by multiplying its local weight with the weight of the superior second-level indicator. The capability values for all states form the capability vector $\mathbf{C} = (c_1, c_2, \ldots, c_N)^{\mathrm{T}}$.

3.3.2. Indicator Normalization and Hierarchical CRITIC Weighting

The min–max normalization method is employed to eliminate dimensional differences. For a benefit-type indicator:

$$y_{sv} = \frac{x_{sv} - \min\limits_{s} x_{sv}}{\max\limits_{s} x_{sv} - \min\limits_{s} x_{sv}} \tag{12}$$

For a cost-type indicator:

$$y_{SV} = \frac{\max\limits_{s} x_{SV} - x_{SV}}{\max\limits_{s} x_{\mathrm{SV}} - \min\limits_{\mathrm{s}} x_{sv}} \tag{13}$$

When a second-level indicator subsumes constant indicators, these are grouped with variable indicators under a strategy of equal-weight base allocation with sensitivity analysis. The base weight of each constant indicator is determined by equally apportioning the total weight among all third-level indicators in that second-level category; a sensitivity scan over

the constant indicators' weights is then performed to verify the robustness of the capability vector **C**. Only data from executable mission states are used in the weight calculation, with zero values from low-energy and failed states excluded, thereby ensuring that the weights objectively reflect the relative importance of the indicators.

For the p_k third-level indicators under the k-th second-level indicator, the CRITIC method proceeds as follows [29]:

(1) Calculate the standard deviation (contrast intensity) of the v-th indicator:

$$\sigma_v = \sqrt{\frac{1}{N-1}\sum_{s=1}^{N}(y_{sv} - \bar{y}_v)^2} \tag{14}$$

(2) Calculate the indicator conflict (mean absolute correlation coefficient):

$$\rho_v = \frac{1}{p_k - 1}\sum_{w \neq v} |r_{wv}| \tag{15}$$

where r_{vw} is the Pearson correlation coefficient between indicators v and w.

(3) Calculate the information content:

$$G_v = \sigma_v \cdot (1 - \rho_v) \tag{16}$$

(4) Determine the local weight:

$$\omega_v = \frac{G_v}{\sum_{u=1}^{p_k} G_u}, \quad \sum_{v=1}^{p_k} \omega_v = 1 \tag{17}$$

The second-level indicators are then treated as composite indicators. Their scores in each state are calculated via Equation (10), and the CRITIC method is reapplied to obtain the second-level weights λ_k. Global weights are synthesized by multiplying the local weights by the corresponding second-level weights and substituting the result into Equation (11) to yield the comprehensive capability value for each joint state. For normal states in which the energy level falls below the effective operational threshold and for all hardware-failed states, the USV cannot accomplish the specified mission owing to insufficient battery power or hardware failure; in accordance with engineering practice and to ensure a conservative and reliable evaluation, the capability value for these states is uniformly set to zero.

4. Case Study and Discussion

4.1. Simulation Parameters and Scenario Settings

4.1.1. Simulation Location and Meteorological Data

Simulations are performed for the Wanshan sea area in the northern South China Sea (21.94° N, 113.65° E). Solar energy input is derived from the hourly solar irradiance sequence for this region over 2021–2023, with superimposed Gaussian random perturbations [30].

4.1.2. USV Platform Parameters and Mission Capability Indicators

The simulation considers a typical inshore solar-powered USV. The basic physical platform parameters and simulation conditions are listed in Table 1, and the mission capability benchmark indices under different energy states are given in Table 2.

Table 1. Basic simulation and platform parameters of the solar-powered USV.

Parameter	Symbol	Value	Unit	Parameter	Symbol	Value	Unit
Photovoltaic Area	A_{PV}	2.7	m^2	Maximum Charging Power	P_{ch}^{max}	0.42	kW
Photovoltaic Efficiency	η_{PV}	0.21	—	Maximum Discharging Power	P_{dis}^{max}	0.35	kW
MPPT Efficiency	η_{MPPT}	0.96	—	Base Load	P_{base}	0.096	kW
Battery Capacity	E_{bat}	4.1	kWh	Task Load	P_{task}	0.100	kW
Minimum SOC	SOC_{min}	0.0	—	Fault Load	P_{fail_load}	0.0	kW
Maximum SOC	SOC_{max}	1.0	—	Average Failure Interval Time	MTBF	1000	h
Charging Efficiency	η_{ch}	0.93	—	Average Repair Time	MTTR	85	h
Discharging Efficiency	η_{dis}	0.96	—	Initial SOC	SOC_{init}	0.5	—

Table 2. Original parameters of mission capability indices under different energy states.

Second-Level Indicator	Third-Level Indicator	Unit	Initial State				Remarks
			X_1	X_2	X_3	X_4	
Maneuvering Capability	Cruise Speed	kn	2.2	2.0	1.7	1.3	Lower speed saves energy at lower SOC
	Maximum Range (Solar Only)	n mile	700	550	380	190	Relies on solar power
	Maximum Range (Hybrid Propulsion)	n mile	1480	1420	1350	1050	Smaller reduction with hybrid propulsion
	Energy Self-Sustainment days	d	15.5	11.5	7.5	3.0	Decreases with energy level
	Turning Radius	m	32	32	32	32	Constant
Detection and Identification Capability	Visible-Light Detection Range	km	4.2	3.2	2.2	1.2	Drops sharply at low energy
	Visible-Light Identification Range	km	1.40	0.70	0.45	0.18	Same trend
	Infrared Detection range	km	2.6	2.1	1.6	1.1	Insufficient cooling degrades performance
	Infrared Identification range	km	1.15	0.95	0.75	0.45	Same as IR detection
	Radar Detection Range (RCS = 1 m^2)	km	2.4	1.9	1.4	0.9	Same trend
	Radar Detection Range (RCS = 0.1 m^2)	km	2.0	1.5	1.0	0.6	Same trend
On-site Evidence Acquisition Capability	Visible-Light Image Resolution	pixel	1920 × 1080	1680 × 1050	1280 × 800	640 × 480	Resolution degrades stepwise
	Infrared Image Resolution	pixel	1280 × 1024	1152 × 864	800 × 600	512 × 384	Reduced resolution at low energy
	Storage Capacity	TB	2	2	2	2	Ultra-low-power storage; constant
Communication and Data Transmission Capability	Maximum Communication Distance (Line-of-Sight)	km	14	11	7	4	Transmit power decreases with energy
	Real-time Transmission Bandwidth	Mbps	2.8	1.8	0.9	0.4	Energy-saving and noise reduction
Autonomous Reconnaissance and Collaboration Capability	Pre-programmed Route Waypoints	points	140	140	90	40	Degraded operation at low energy
	Maximum Number of Collaborative Vessels	vessels	7	5	3	1	Collaboration energy decreases
	Abnormal Target Alarm Delay	s	85	85	105	125	Processing delay increases at low energy

4.2. Solution of the Availability Vector

To eliminate transient errors arising from the initial simulation conditions, a one-year (8760 h) warm-up procedure was implemented. This enabled the coupled energy–reliability system of the USV to detach from the initial constraints and settle into a natural steady state. After the warm-up, the mean and standard deviation of the daily mission-start SOC were tracked over a subsequent continuous 730-day mission period (Figure 4). The black curve corresponds to the time series of single-day initial SOCs; the steady-state mean of 0.19525 is markedly distinct from the artificially prescribed initial value of 0.5 (Figure 5). The red curve represents the standard deviation sequence, which levels off at an average of 0.01854, indicating a fluctuation amplitude that is exceedingly low. These results demonstrate that, following the full warm-up period, the system has completely shed the influence of the initial SOC assignment and reached a long-term energy equilibrium. This equilibrium is dictated jointly by the insolation environment, load power, and hardware reliability constraints. The small standard deviation further confirms that energy fluctuations under steady state are tightly bounded and that the system operates in a highly stable regime. Accordingly, all subsequent effectiveness evaluations, probability statistics, and state transition matrix calculations are based on this post-warm-up steady-state initial distribution, thereby rigorously ensuring the objectivity and engineering credibility of the assessment outcomes.

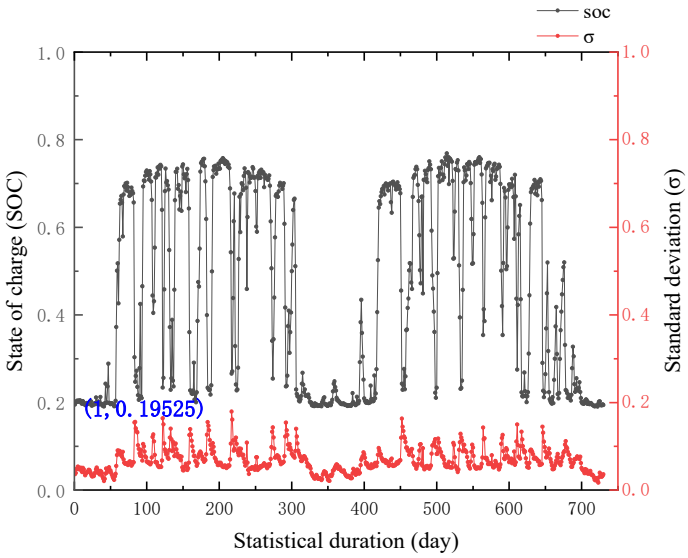


Figure 4. Time variation in daily initial SOC and its standard deviation during the statistical period.

Convergence verification based on 1000 Monte Carlo repetitions is presented in Figures 6 and 7. Both the mission-start average SOC and the system availability stabilize rapidly as the number of iterations increases. Specifically, the sliding-window coefficient of variation decays monotonically toward zero. This statistically confirms that 1000 runs provide sufficient convergence and that the derived initial probability distribution is robust for subsequent modelling.

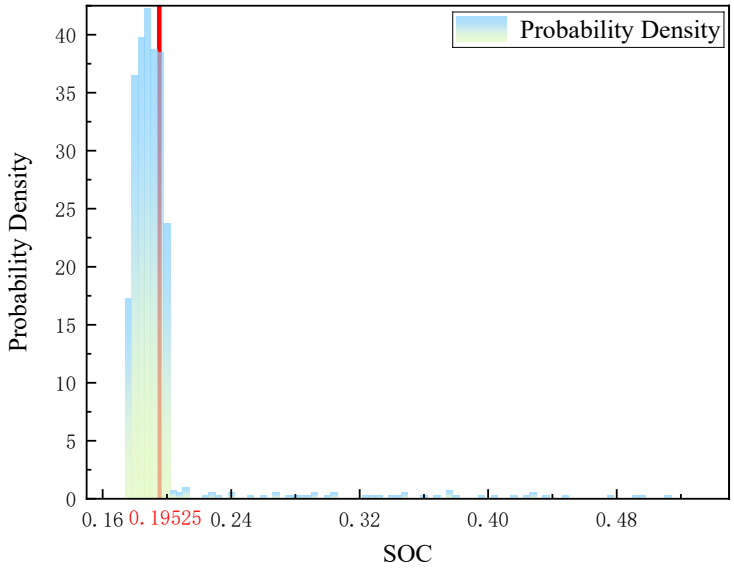


Figure 5. Probability density function of initial SOC derived from 1000 Monte Carlo repetitions.

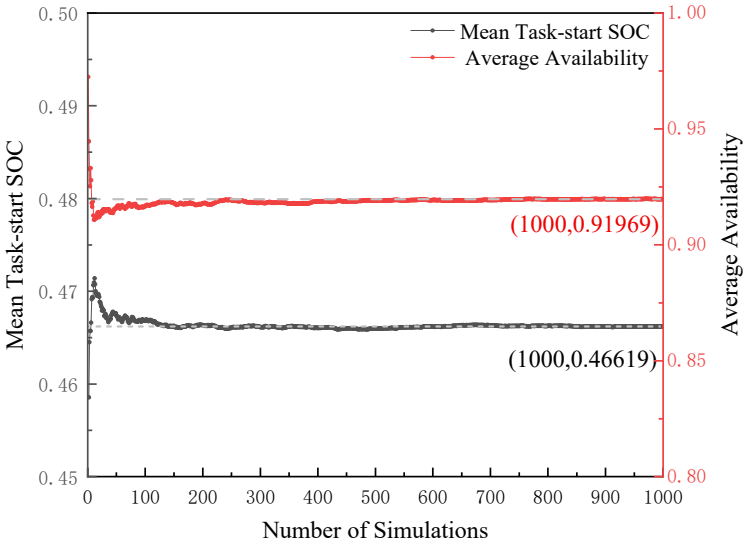


Figure 6. Convergence curves of SOC mean and system availability under multiple simulations.

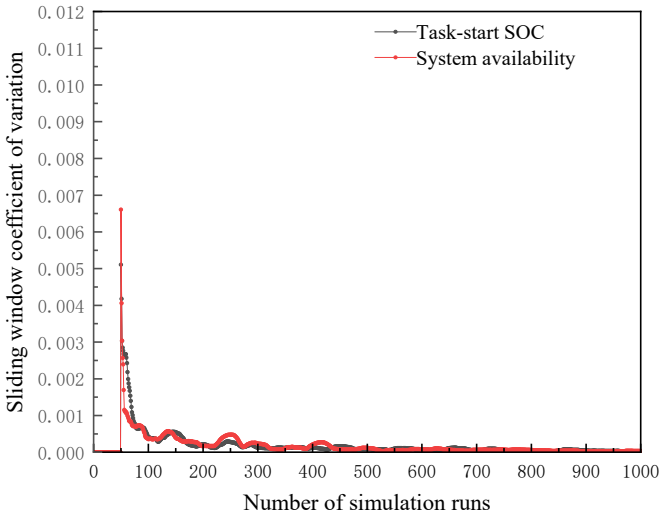


Figure 7. Convergence characteristic of the sliding-window coefficient of variation.

Based on the steady-state validation and convergence checks, raw occurrence counts of hardware–energy joint states are tallied across the 1000 converged simulation trials and normalized to derive the steady-state probability distribution (Figure 8). The resultant distribution features a dominant peak at state X_1, followed by a secondary local maximum around X_4. Probabilities decline gradually from X_1 toward X_5 and drop sharply for states X_6–X_{10}. This overall distribution is consistent with the steady-state behaviour expected from the initial parameter settings of the system.

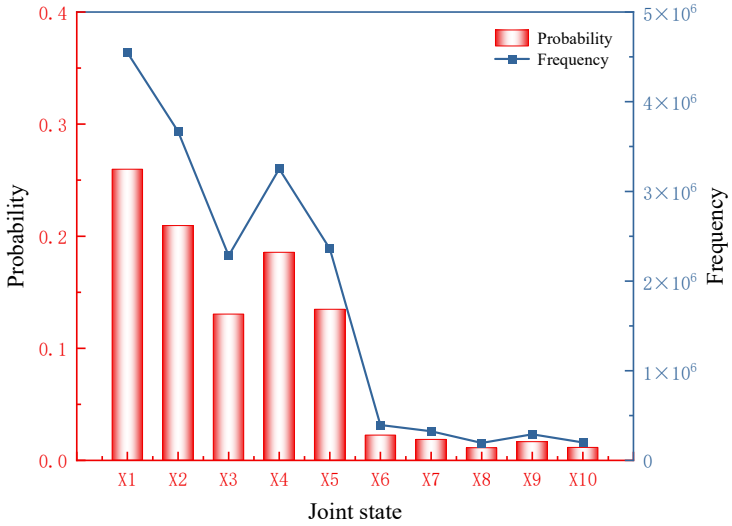


Figure 8. Probability distribution of the hardware–energy combined steady states.

The resulting initial availability vector is:

$$A = [0.259655, 0.209397, 0.130339, 0.185589, 0.134712, 0.022510, 0.018526, 0.011168, 0.016655, 0.011449] \quad (18)$$

These statistical results indicate that, under steady state, the system hardware availability reaches approximately 91.97%, while the failure proportion is approximately 8.03%; concurrently, energy levels remain stably within the medium-to-high range. This distribution closely matches the initial parameter settings of the system.

In summary, the warm-up debiasing, convergence verification, and probability statistics together yield an availability vector that eliminates initial transient errors, faithfully reflects the steady-state characteristics of the USV mission, and supplies a credible, high-precision input for subsequent mission-effectiveness calculations.

4.3. Solution of the Dependability Transition Probability Matrix

For a typical mission duration of 10 h (08:30–18:30), the steady-state availability vector A is taken as the initial distribution. Transition frequencies of the joint states are counted via Monte Carlo simulation under the same irradiance and platform parameters, with the task load applied. After normalization, the 10th-order transition probability matrix D is obtained:

$$D = \begin{bmatrix} 0.9903 & 0.0073 & 0.0020 & 0.0000 & 0.0000 & 0.0003 & 0.0000 & 0.0000 & 0.0000 & 0.0000 \\ 0.8763 & 0.0572 & 0.0570 & 0.0004 & 0.0000 & 0.0057 & 0.0032 & 0.0001 & 0.0000 & 0.0000 \\ 0.4258 & 0.4112 & 0.1114 & 0.0390 & 0.0031 & 0.0023 & 0.0034 & 0.0036 & 0.0001 & 0.0000 \\ 0.0000 & 0.0750 & 0.4504 & 0.3801 & 0.0850 & 0.0000 & 0.0007 & 0.0035 & 0.0052 & 0.0002 \\ 0.0000 & 0.0000 & 0.0423 & 0.3104 & 0.6377 & 0.0000 & 0.0000 & 0.0005 & 0.0044 & 0.0047 \\ 0.0000 & 0.0000 & 0.0000 & 0.0000 & 0.0000 & 1.0000 & 0.0000 & 0.0000 & 0.0000 & 0.0000 \\ 0.0000 & 0.0000 & 0.0000 & 0.0000 & 0.0000 & 0.0000 & 1.0000 & 0.0000 & 0.0000 & 0.0000 \\ 0.0000 & 0.0000 & 0.0000 & 0.0000 & 0.0000 & 0.0001 & 0.0003 & 0.9996 & 0.0000 & 0.0000 \\ 0.0000 & 0.0000 & 0.0000 & 0.0000 & 0.0000 & 0.0000 & 0.0000 & 0.0001 & 0.9999 & 0.0000 \\ 0.0000 & 0.0000 & 0.0000 & 0.0000 & 0.0000 & 0.0000 & 0.0000 & 0.0000 & 0.0002 & 0.9998 \end{bmatrix} \quad (19)$$

Figure 9 presents the mean heatmap of the transition matrix D. The matrix is diagonally dominant, indicating that within a single task step the system has the highest probability of remaining in its current state, which reflects robust operational behaviour. In the bottom-right fault subspace, the probability is strongly concentrated on the diagonal. This demonstrates that once a fault occurs, the system ceases photovoltaic power generation and persists in the faulty state, consistent with the model formulation. The bottom-left submatrix, which governs transitions from faulty to healthy states, is entirely zero, confirming at the data level that hardware faults are irreversible over short-duration missions.

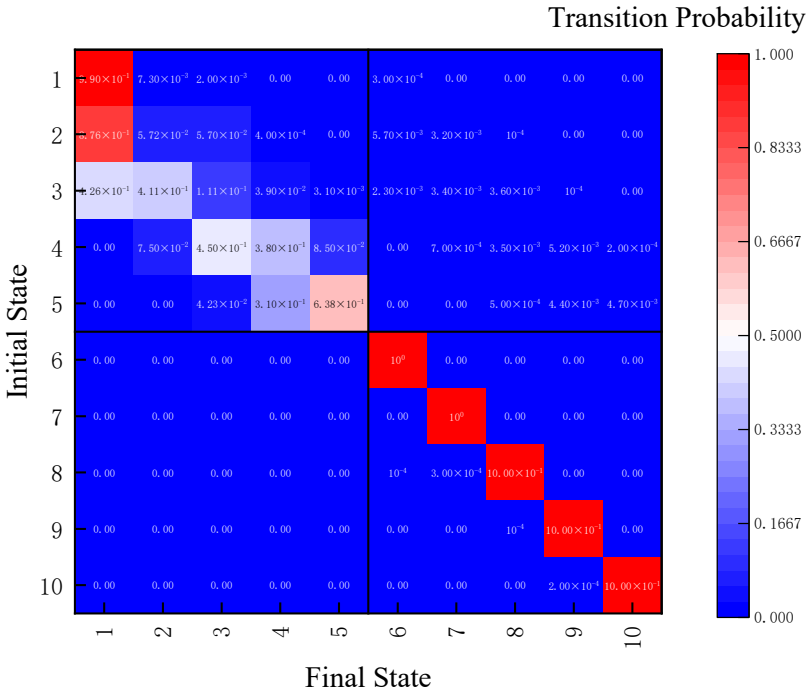


Figure 9. Mean heatmap of the combined state transition probability.

Figure 10 presents the standard-deviation heatmap of the joint-state transition probabilities, computed from 1000 independent stochastic simulation runs. The ensemble-averaged standard deviation across all transition entries is only 0.00748. This uniformly low statistical dispersion confirms the numerical stability and convergence of the derived transition probability matrix. It further demonstrates that the proposed modelling framework yields statistically robust and credible estimates of transition probabilities.

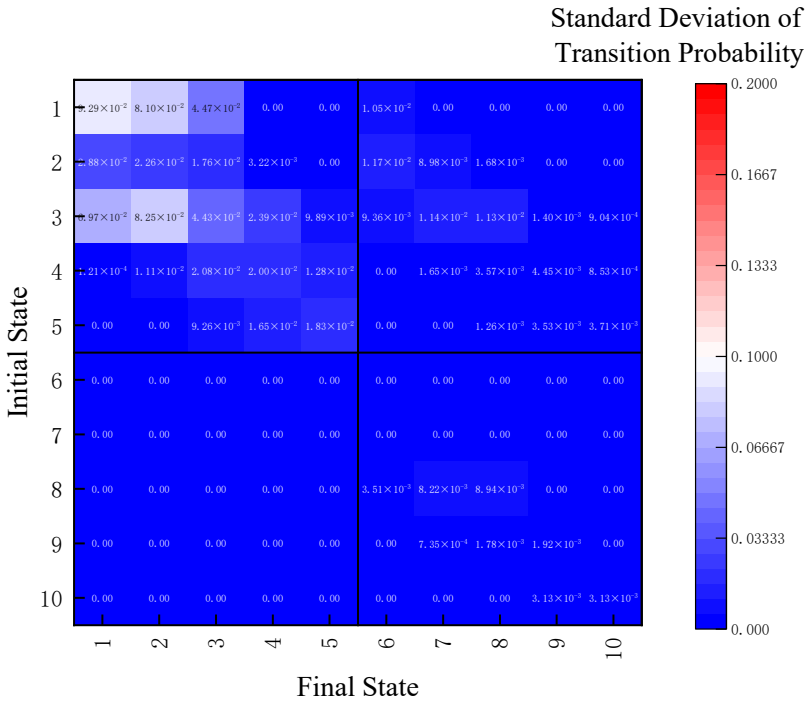


Figure 10. Standard deviation heatmap of the combined state transition probability.

The Frobenius norm convergence curve (Figure 11) demonstrates that the norm error decays rapidly and stabilizes at 1000 runs, confirming sufficient sample size.

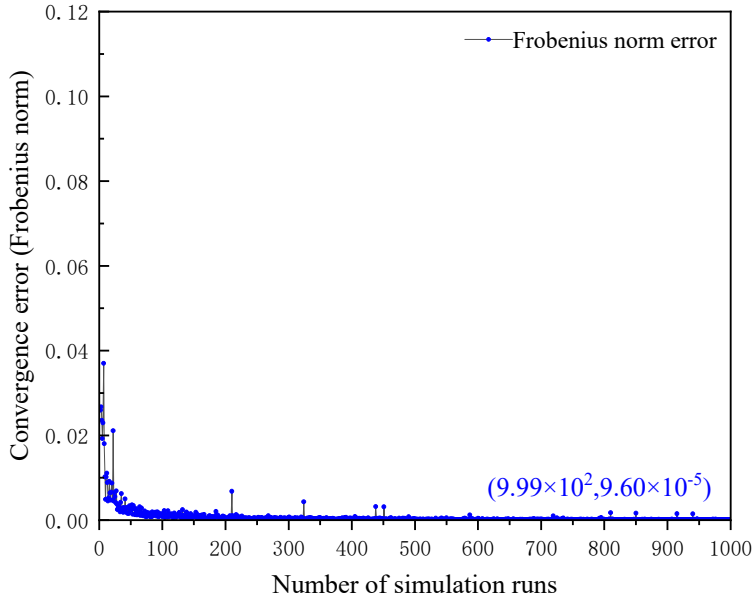


Figure 11. Global convergence error curve based on the Frobenius norm.

4.4. Solution of the Capability Vector

After min–max normalization, all indicators are mapped to [0, 1]. The normalized matrix **Y** for the 19 third-level indicators under the four normal operating states X_1–X_4 serves as the basis for hierarchical CRITIC weighting and capability synthesis.

$$Y^T = \begin{bmatrix} 1.0000 & 1.0000 & 1.0000 & 1.0000 & 1.0000 & 1.0000 & 1.0000 & 1.0000 & 1.0000 & 1.0000 \\ 0.9091 & 0.7857 & 0.9595 & 0.7419 & 1.0000 & 0.7619 & 0.5000 & 0.8077 & 0.8261 & 0.7917 \\ 0.7727 & 0.5429 & 0.9122 & 0.4839 & 1.0000 & 0.5238 & 0.3214 & 0.6154 & 0.6522 & 0.5833 \\ 0.5909 & 0.2714 & 0.7095 & 0.1935 & 1.0000 & 0.2857 & 0.1286 & 0.4231 & 0.3913 & 0.3750 \\ 1.0000 & 1.0000 & 1.0000 & 1.0000 & 1.0000 & 1.0000 & 1.0000 & 1.0000 & 1.0000 & \\ 0.7500 & 0.8507 & 0.7594 & 1.0000 & 0.7857 & 0.6429 & 1.0000 & 0.7143 & 1.0000 & \\ 0.5000 & 0.4938 & 0.3662 & 1.0000 & 0.5000 & 0.3214 & 0.6429 & 0.4286 & 0.5000 & \\ 0.3000 & 0.1481 & 0.1500 & 1.0000 & 0.2857 & 0.1429 & 0.2857 & 0.1429 & 0.0000 & \end{bmatrix} \quad (20)$$

The rows of the matrix correspond to the energy states X_1, X_2, X_3, X_4, respectively, while the columns correspond to the tertiary evaluation indicators in Table 2.

Taking "Maneuvering Capability" as an example, its five third-level indicators include four variable ones and one constant (turning radius). Applying the CRITIC method described in Section 3.3, the weights for the variable indicators are summarized in Table 3.

Table 3. CRITIC weights of variable indicators under maneuvering capability.

Third-Level Indicator	Standard Deviation σ_v	Average Correlation Coefficient ρ_v	Information Gain G_v	CRITIC Weight
Cruise speed	0.1780	0.7378	0.1866	0.1786
Maximum Range (Solar Only)	0.3140	0.7332	0.3351	0.3207
Maximum Range (Hybrid Propulsion)	0.1290	0.7080	0.1506	0.1442
Energy Self-Sustainment Days	0.3458	0.7308	0.3724	0.3564

The local weights are assigned as: variable indicators share 4/5 = 0.8 of the total weight, distributed according to their CRITIC weights; the constant indicator receives 1/5 = 0.2. The final local weights are listed in Table 4.

Table 4. Local weights of third-level indicators for maneuvering capability.

Third-Level Indicator	Local Weight ω_v
Cruise Speed	0.1429
Maximum Range (Solar Only)	0.2566
Maximum Range (Hybrid Propulsion)	0.1154
Energy Self-Sustainment Days	0.2851
Turning Radius	0.2000
Total	1.0000

Following the same procedure, calculate the local weights for the third-level indicators under each second-level indicator; the summarized results are presented in Table 5.

Table 5. Local weights of tertiary indicators under each secondary indicator.

Secondary Indicator	Tertiary Indicator	Local Weight
Maneuvering Capability	Cruise Speed	0.1429
	Maximum Range (Solar Only)	0.2566
	Maximum Range (Hybrid Propulsion)	0.1154
	Energy Self-Sustainment Days	0.2851
	Turning Radius	0.2000
Detection and Identification Capability	Visible-Light Detection Range	0.1682
	Visible-Light Identification Range	0.2341
	Infrared Detection Range	0.1358
	Infrared Identification Range	0.1483
	Radar Detection Distance (RCS = 1 m^2)	0.1471
	Radar Detection Distance (RCS = 0.1 m^2)	0.1665
On-Site Evidence Acquisition Capability	Visible-Light Image Resolution	0.3328
	Infrared Image Resolution	0.3338
	Storage Capacity	0.3333
Communication and Data Transmission Capability	Maximum Communication Distance	0.4543
	Real-Time Transmission Bandwidth	0.5457
Autonomous Reconnaissance and Collaboration Capability	Pre-programmed Route Waypoints	0.2828
	Max number of collaborative vessels	0.3213
	Abnormal target alarm delay	0.3959

Using the local weights of the tertiary indicators from Table 5 and applying Equation (10), the scores of the secondary indicators under various conditions are calculated. The results are summarized in Table 6.

Table 6. Scores of secondary indicators under different normal states.

Condition	Maneuvering Capability	Detection and Identification Capability	On-Site Evidence Acquisition Capability	Communication and Data Transmission Capability	Autonomous Reconnaissance and Collaboration Capability
X_1	1.0000	1.0000	1.0000	1.0000	1.0000
X_2	0.8538	0.7187	0.8700	0.7078	0.9082
X_3	0.6929	0.5127	0.6200	0.4026	0.5175
X_4	0.4911	0.2988	0.4327	0.2078	0.1267

Based on Table 6 and using the CRITIC objective weighting method described in Section 3.3, the final objective weights of the secondary indicators are determined. The results are summarized in Table 7.

Table 7. Weights of secondary indicators.

Secondary Indicator	Standard Deviation σ_v	Average Correlation Coefficient ρ_v	Information Gain G_v	CRITIC Weight
Maneuvering Capability	0.4293	0.7908	0.4492	0.1901
Detection and Identification Capability	0.4264	0.7843	0.4599	0.1947
On-Site Evidence Acquisition Capability	0.4471	0.7908	0.4677	0.1980
Communication and Data Transmission Capability	0.4389	0.7851	0.4717	0.1996
Autonomous Reconnaissance and Collaboration Capability	0.4580	0.7755	0.5141	0.2176

By weighting and combining the secondary indicator weights with the corresponding local weights of the tertiary indicators, the global weights of the tertiary indicators are determined. The results are summarized in Table 8.

Table 8. Global weights of tertiary indicators.

Secondary Indicator	Tertiary Indicator	Global Weight
Maneuvering Capability (0.1901)	Cruise Speed	0.0272
	Maximum Range (Solar Only)	0.0488
	Maximum Range (Hybrid Propulsion)	0.0219
	Energy Self-Sustainment Days	0.0542
	Turning Radius	0.0380
Detection and Identification Capability (0.1947)	Visible-Light Detection Range	0.0327
	Visible-Light Identification Range	0.0456
	Infrared Detection Range	0.0264
	Infrared Identification Range	0.0289
	Radar Detection Distance (RCS = 1 m^2)	0.0286
	Radar Detection Distance (RCS = 0.1 m^2)	0.0324
On-Site Evidence Acquisition Capability (0.1980)	Visible-Light Image Resolution	0.0659
	Infrared Image Resolution	0.0661
	Storage Capacity	0.0660
Communication and Data Transmission Capability (0.1996)	Maximum Communication Distance	0.0907
	Real-Time Transmission Bandwidth	0.1089
Autonomous Reconnaissance and Collaboration Capability (0.2176)	Pre-programmed Route Waypoints	0.0615
	Max number of collaborative vessels	0.0699
	Abnormal target alarm delay	0.0862
Total		1.0000

Using the method described in Section 3.3, the system capability vector is obtained as:

$$C = [1.0000, 0.8134, 0.5472, 0.3062, 0, 0, 0, 0, 0, 0]^T$$

The constant indicators have already obtained non-zero global weights during the weighting process. To quantitatively analyze the disturbance effect of these indicator weight fluctuations on the capability evaluation ranking and effectiveness assessment conclusions, this paper proposes four scenarios with varying weight perturbations for sensitivity analysis.

Scenario A (Base Case): The constant indicators retain their original weight assignments.

Scenario B (Low Constant Weight Case): The total weight of the constant indicators is reduced to 50% of their original value, while the weights of the other variable tertiary indicators are proportionally increased to maintain overall weight normalization.

Scenario C (High Constant Weight Case): The total weight of the constant indicators is increased to 150% of their original value. The weights of the other variable tertiary indicators are proportionally decreased to keep the overall weight normalized.

In this scenario, the system's capability is calculated solely based on the variable indicators.

Scenario D (No Constant Weight Case): The influence of the constant indicators is completely eliminated, similar to the traditional CRITIC objective weighting method. The comprehensive system capability values for scenarios $X_1 \sim X_4$ are calculated under each of the four weight schemes. The statistical results are presented in Table 9.

Table 9. Comparison of capability values under different weights of constant indicators.

Condition	Scenario A (Base)	Scenario B (Low Constant)	Scenario C (High Constant)	Scenario D (Zero Constant)
X_1	1.0000	1.0000	1.0000	1.0000
X_2	0.8134	0.8035	0.8233	0.7936
X_3	0.5472	0.5211	0.5733	0.4950
X_4	0.3062	0.2661	0.3464	0.2259

As shown in Table 9, under each set of weight perturbations, the ranking of capability values remains stable, consistently satisfying

$$X_1 > X_2 > X_3 > X_4 \quad (21)$$

with no significant fluctuations in the difference between them.

In Scenario A (baseline), X_1 yields a capability score of 1.0000 and remains invariant across all weight-perturbation scenarios. The score of X_2 is 0.8134 in Scenario A. It decreases slightly to 0.8035 in Scenario B (low constant weight), rises slightly to 0.8233 in Scenario C (high constant weight), and falls to 0.7936 in Scenario D (zero constant weight), yielding an overall fluctuation within $\pm 2.4\%$. X_3 has a baseline score of 0.5472 and varies between 0.4950 and 0.5733 across the four scenarios, a fluctuation somewhat wider than that of X_2; its relative ranking, however, remains unchanged. X_4 is the most sensitive to weight changes. Its baseline score of 0.3062 drops to 0.2259 in Scenario D and increases to 0.3464 in Scenario C, exhibiting the largest numerical variation among the four schemes. Nevertheless, it consistently holds the lowest capability ranking in all scenarios.

These sensitivity results confirm that the relative ranking of capability scores is stable under different weight perturbations, demonstrating strong robustness. Thus, the proposed hierarchical CRITIC weighting method effectively captures the intrinsic importance of the indicators, and the resulting effectiveness evaluation is not strongly sensitive to the pre-assigned weights of the constant indicators. Owing to the weighted aggregation logic of the model, and to the fact that the state transition and steady-state distribution matrices inherently favour high-energy scenarios, adjusting the constant-indicator weights produces only a linear scaling of the effectiveness results for each scheme. The relative effectiveness hierarchy among both schemes and scenarios remains unchanged.

In summary, the baseline scenario constructed in this work is robust in its parameter settings and stable in its evaluation outcomes. It therefore provides a reliable foundation for subsequent effectiveness projection and scheme comparison.

4.5. Efficiency Calculation

Based on the ADC model framework and by substituting the numerical results obtained from Section 4.2 to Section 4.4, the baseline task efficiency is calculated as:

$$E = 0.661934 \quad (22)$$

To quantitatively isolate the independent contributions of energy state dynamics and hardware random failures to efficiency evaluation, two control simulation scenarios are established:

Scenario One: Only hardware failures are considered, with energy dynamics excluded. It is assumed that the battery's state of charge (SOC) does not decrease throughout the mission, all normal hardware operates at peak capacity, and the logic and probabil-

ity of hardware failures remain unchanged. Under these assumptions, the efficiency is calculated as:

$$\begin{aligned} E_{noEnergy} &= \sum_{i=1}^{5} A_i \times 1.0000 \\ &= 0.919692 \times 1.0000 = 0.919692 \end{aligned} \tag{23}$$

Scenario Two: Hardware random failures are ignored (only energy dynamics are considered). It is assumed that the hardware system is absolutely reliable throughout the mission and no failure transitions occur. Using the simulation framework developed in this paper, a Monte Carlo simulation is rerun to obtain the energy level distribution at the initial moment of the mission when the hardware is in a normal state. After normalization, the initial state vector is obtained:

$$A_{\text{norm}} = \begin{bmatrix} 0.282384 & 0.227307 & 0.140491 & 0.202596 & 0.147222 \end{bmatrix} \tag{24}$$

A 5×5 credibility submatrix that includes only energy transitions between normal states is constructed:

$$D_{HH} = \begin{bmatrix} 1.0000 & 0.0000 & 0.0000 & 0.0000 & 0.0000 \\ 0.8880 & 0.0540 & 0.0579 & 0.0000 & 0.0000 \\ 0.4482 & 0.4017 & 0.1126 & 0.0374 & 0.0000 \\ 0.0000 & 0.0740 & 0.4548 & 0.3855 & 0.0858 \\ 0.0000 & 0.0000 & 0.0435 & 0.3134 & 0.6431 \end{bmatrix} \tag{25}$$

The task capability vector consists of the first 5 components of the original capability vector C that correspond to the normal hardware state, denoted as:

$$C_H = [1.0000, 0.8134, 0.5472, 0.3062, 0]^T \tag{26}$$

Substituting these values into the efficiency calculation formula:

$$E_{\text{NoFailure}} = A_{\text{norm}} \cdot D_{\text{HH}} \cdot C_{\text{H}} = 0.724717 \tag{27}$$

By comparing the differences between the three scenarios, the independent impacts of "energy state dynamics" and "hardware random failures" on the efficiency of the solar-powered unmanned boat can be quantitatively analyzed.

When energy-state dynamics are ignored, the evaluated mission effectiveness reaches 0.919692, which is 38.94% above the baseline value. This substantial overestimation demonstrates that neglecting real-time SOC attenuation and adopting a fixed full-energy assumption markedly exaggerates the operational capability of solar-powered USVs. Ongoing onboard power consumption gradually depletes stored electrical energy, while intermittent solar photovoltaic generation cannot fully offset the cumulative energy deficit over the mission horizon. Time-varying energy evolution thus constitutes the dominant constraint on overall mission performance.

Excluding random hardware failures yields an effectiveness value of 0.724717, corresponding to a 9.48% upward deviation from the baseline result. At a steady-state hardware failure proportion of approximately 8%, this non-negligible failure rate eliminates the mission contribution of all affected subsystems. The gap between the 9.48% and 38.94% deviations reflects the dominant constraint imposed by dynamic energy depletion, not the insignificance of hardware effects. Hardware degradation therefore introduces a tangible negative contribution to mission effectiveness that cannot be disregarded, even though it is secondary to energy-induced performance reduction. This finding further

reinforces the necessity of integrating both hardware health and battery SOC within the proposed ADC evaluation framework.

4.6. Discussion on Framework Scalability

Beyond the solar-powered USV case validated in this study, the proposed joint state-space ADC evaluation framework is designed for cross-platform transferability to other renewable-energy-operated marine vehicle systems. This transferability stems from the decoupling of the core effectiveness evaluation paradigm from the specific energy supply form.

Architecturally, the framework comprises a general underlying layer and a replaceable energy layer. The general underlying layer integrates the binary-state hardware reliability modelling method, the unified joint state-space construction logic, the ADC three-dimensional effectiveness calculation procedure, and the hierarchical capability weighting scheme. These components serve renewable-energy unmanned marine platforms independently of the energy input form. The replaceable energy layer encompasses the renewable-energy input stochastic model and the energy state transition rules, and can be tailored to the energy conversion characteristics of different power supply modes, avoiding repeated redevelopment of the core evaluation architecture.

For wind-powered unmanned surface vehicles, the primary adjustment is replacing the solar irradiance stochastic model with a wind-speed random process model and revising the power generation calculation according to the wind turbine power curve; the hardware state modelling, SOC state transition mechanism, and capability evaluation system can be inherited directly. For wave-energy-powered marine platforms, the wave energy capture power model must be reconstructed to match the wave height and period distribution characteristics, and the energy state discretisation interval should be adjusted to account for the lower energy density and stronger output fluctuation. For marine vehicles with hybrid renewable energy systems such as solar–wind complementary power supply, the core evaluation framework is retained, but multi-energy cooperative scheduling logic must be added in the energy state transition step, and supplementary indicators such as energy supply stability should be introduced in the capability dimension to capture the complementary benefits of multiple energy sources.

This transferability allows the framework to extend beyond a single energy form toward a unified mission effectiveness evaluation system for multiple types of renewable-energy marine unmanned platforms. In engineering practice, the framework can provide a consistent quantitative benchmark for comparing alternative renewable-energy power supply configurations, particularly during the conceptual design and scheme evaluation stage of new marine unmanned platforms.

5. Conclusions

This study addresses the coupled constraints that dynamic hardware condition and time-varying stochastic energy supply jointly impose on the mission effectiveness of solar-powered USVs. An enhanced ADC evaluation framework is developed, built upon a novel joint state-space model that integrates hardware condition and battery SOC. In contrast to the binary healthy/faulty state simplification of conventional ADC theory, the proposed unified state space jointly encodes hardware condition and discretised battery SOC. This enables precise quantification of energy-coupled performance degradation throughout mission execution.

Using measured regional solar irradiance data, a Monte Carlo simulation incorporating an extended warm-up procedure is implemented to compute the steady-state initial joint-state probability distribution for the availability vector. This approach eliminates the

arbitrary assignment of a preset initial SOC and endows the availability calculation with physically meaningful input. The derived state transition matrix couples stochastic hardware failure occurrences with continuous battery charge–discharge dynamics. Numerical simulations verify three properties central to the modelling assumptions: the irreversibility of in-mission hardware failure; the tendency of the SOC distribution and subsequent state transitions to shift toward medium and low energy ranges; and the statistical independence of hardware failure probability from onboard energy reserves. A three-layer evaluation indicator system comprising five secondary and nineteen tertiary metrics is established for the capability dimension. An improved hierarchical CRITIC weighting algorithm is employed to achieve fully objective indicator weighting, free from expert subjective bias. Sensitivity tests confirm that state-specific mission capability declines monotonically with decreasing SOC, that all hardware-failed states result in complete loss of execution capability, and that minor perturbations of the constant-indicator weights do not alter the inherent ordering of state capability. These results collectively affirm the robustness of the proposed capability quantification scheme.

Several limitations should be considered when interpreting these findings. First, the binary-state irreparable reliability model is a simplified abstraction of actual hardware behaviour; it does not capture multi-component graded faults, gradual performance degradation, or degraded operational modes under partial system failures. Second, the quantitative analysis was conducted on a single small solar-powered USV platform, and the relative contributions of energy attenuation and hardware failure may differ for platforms with different load levels, PV-to-hull area ratios, and energy storage capacities. Third, the simulation is driven by typical meteorological data from the Wanshan sea area, and mission effectiveness characteristics will vary across sea areas with distinct irradiance patterns and marine environmental conditions. These constraints define the applicable scope of the present findings, and targeted parameter calibration is required before generalizing to other scenarios.

Future work will focus on introducing a state-output feedback mechanism to bridge the gap between effectiveness evaluation and operational control, thereby forming a closed-loop system for mission execution. Real-time system states, including battery SOC, hardware health status, and photovoltaic power generation, will serve as feedback outputs transmitted to the onboard energy management controller and mission scheduling system. Based on the real-time effectiveness level derived from the evaluation model, the controller will dynamically adjust sailing speed, payload power, and route planning. When the energy state is sufficient and the hardware is healthy, mission intensity will be increased to maximize mission return; when the SOC drops below a threshold or a hardware degradation trend is detected, non-essential loads will be shed and sailing speed will be reduced to suppress further performance degradation. Through this closed-loop mechanism of real-time state perception, effectiveness evaluation, feedback regulation, and state updating, the adverse effects of energy depletion and random hardware failures on mission accomplishment can be actively mitigated, rather than merely assessed after the fact.

Building on this foundation, the research will be extended in two complementary directions. First, the modular joint state-space ADC framework will be adapted to other renewable-energy-operated marine vehicle systems, including wind-powered and wave-powered unmanned platforms, by reconstructing the corresponding energy input stochastic models and state transition rules. Second, the reliability model will be refined by incorporating graded hardware degradation and time-varying marine environmental disturbances to improve the precision of state perception and feedback adjustment. The framework will also be validated across additional platform types and sea areas to enhance its practical applicability and generalisability.

Author Contributions: Conceptualization, Y.L., F.M. and Y.S.; methodology, Y.L. and J.Z.; software, Y.L.; validation, Y.L. and J.Z.; formal analysis, Y.L. and C.S.; investigation, Y.L., J.Z. and C.S.; resources, Y.L., C.S. and F.M.; data curation, Y.L., C.S. and Y.S.; data collected and analyzed, Y.L. and J.Z.; writing—original draft preparation, Y.L.; writing—review and editing, Y.S.; visualization, Y.L. and C.S.; supervision, F.M. and Y.S.; project administration, F.M.; funding acquisition, F.M. All authors have read and agreed to the published version of the manuscript.

Funding: This research was funded by the Naval Weaponry and Equipment Comprehensive Research Project (2026102110) and the Autonomous Research Project of the Naval University of Engineering (2026502250).

Data Availability Statement: The regional hourly irradiance dataset used in this study is openly available from the Photovoltaic Geographical Information System (PVGIS) of the European Commission's Joint Research Centre at https://re.jrc.ec.europa.eu/pvg_tools/en/#MR (accessed on 30 May 2026).

Acknowledgments: The authors thank the anonymous reviewers and the editors for their valuable comments and suggestions to improve the quality of this paper. During the preparation of this work, I used DeepSeek (DeepSeek-V4) for two purposes: (1) language polishing and grammar checking to improve the manuscript's readability; and (2) generating code snippets to assist in data processing and analysis. After using this tool, the authors reviewed and edited all AI-assisted content as needed and take full responsibility for the final content of the publication and the integrity of the code.

Conflicts of Interest: The authors declare no conflicts of interest.

References

1. Wang, G.; Xu, T.; Yang, M.; Niu, W. Review on renewable energy systems of unmanned marine vehicles and guidance for energy selection. *Renew. Sustain. Energy Rev.* **2025**, *224*, 116085. [CrossRef]
2. Minak, G. Solar Energy-Powered Boats: State of the Art and Perspectives. *J. Mar. Sci. Eng.* **2023**, *11*, 1519. [CrossRef]
3. Xue, S.; Gao, Y.; Zhang, W.; Sun, Y.; Qin, X. UAV combat effectiveness evaluation based on improved ADC model by bayesian network. *Fire Control Command Control* **2025**, *50*, 49–56. [CrossRef]
4. Zhang, T.; Lü, W.; Li, G. Combat effectiveness evaluation and analysis of air defense system based on improved ADC method. *Fire Control Command Control* **2021**, *46*, 107–113+120. [CrossRef]
5. Chang, H.; Qin, D.; Sun, S.; Wang, S. Operational effectiveness evaluation of marine unmanned aerial vehicle based on ADC model optimization. *J. Ordnance Equip. Eng.* **2023**, *44*, 58–68. [CrossRef]
6. He, S.; Guo, Q.; Wang, X.; Cheng, J.; Chen, Y.; Mao, Y. UAV performance evaluation method optimized based on ADC analysis method. *Unmanned Syst. Technol.* **2022**, *5*, 106–116. [CrossRef]
7. Tang, S.; Fan, P.; Zhang, C.; Zou, J. System effectiveness evaluation of acoustic glider based on optimized ADC model. *J. Unmanned Undersea Syst.* **2025**, *33*, 581–588. [CrossRef]
8. Muzakkir Quamar, M.; Nasir, A.; ELFerik, S. Fault tolerant mission management for UAV under random threat using Markov decision process. *Veh. Commun.* **2025**, *55*, 100959. [CrossRef]
9. Sharma, P.; Atkins, E. Prognostics-informed battery reconfiguration in a multi-battery small UAS energy system. In Proceedings of the 2021 International Conference on Unmanned Aircraft Systems (ICUAS), Athens, Greece, 15–18 June 2021; pp. 423–432. [CrossRef]
10. Bi, W.; Gao, F.; Zhang, A. A novel weapon system effectiveness assessment method based on the interval-valued evidential reasoning algorithm and the analytical hierarchy process. *IEEE Access* **2021**, *9*, 53480–53490. [CrossRef]
11. Yang, Y.; Xu, S.; Chen, M.; Cui, G.; Hu, J. Quantitative characterization of reservoir heterogeneity using the AHP-CRITIC method: A case study of the 24 layer of Es4scx submember in Block Fan 151. *Bull. Geol. Sci. Technol.* **2026**, *45*, 68–77. [CrossRef]
12. Xu, T.; Liu, X.; Zhang, Z. Simplified likelihood estimation of ship total loss using GRA and CRITIC methods. *Transp. Plan. Technol.* **2020**, *43*, 223–236. [CrossRef]
13. Lamas, M.I.; Castro-Santos, L.; Rodriguez, C.G. Optimization of a Multiple Injection System in a Marine Diesel Engine through a Multiple-Criteria Decision-Making Approach. *J. Mar. Sci. Eng.* **2020**, *8*, 946. [CrossRef]
14. Dai, J.; Fang, J.; Zheng, S.; Ouyang, Y. Evaluation and Prediction of Big Data-Driven Marine Ecological Restoration Effect Based on CRITIC-IGA Hybrid Model. *J. Mar. Sci. Eng.* **2025**, *13*, 2241. [CrossRef]
15. Zheng, J.; Yang, G. Efficiency analysis method of surface ship combat system based on ADC model. *Ship Electron. Eng.* **2017**, *37*, 18–21. [CrossRef]

16. Zhu, D.; Shi, Q.; Tan, S.; Xiong, F.; Shi, X. Research on safeguarding effectiveness evaluation renovation of military and civil fusion equipment based on ADC-neural network. *Math. Pract. Theory* **2025**, *55*, 248–255. [CrossRef]
17. Manohar, P.; Atla, C.R. Development of predictive reliability model of solar photovoltaic system using stochastic diffusion process for distribution system. *IEEE J. Emerg. Sel. Top. Circuits Syst.* **2022**, *12*, 279–289. [CrossRef]
18. Shah, S. Monte Carlo simulation in renewable energy planning: A comprehensive review and novel framework for uncertainty quantification. *Am. J. Eng. Technol.* **2025**, *7*, 24–45. [CrossRef]
19. Zhu, J.; Chen, L. Stochastic Optimization of Onboard Photovoltaic Hybrid Power System Considering Environmental Uncertainties. *J. Mar. Sci. Eng.* **2024**, *12*, 1240. [CrossRef]
20. Corsi, P.; Jakovlev, S.; Figari, M.; Djackov, V. A Stochastic Approach for Evaluating the Reliability of a MASS and Assessing the Compliance with the IMO Regulatory Framework. *J. Mar. Sci. Eng.* **2026**, *14*, 814. [CrossRef]
21. Xiang, C.; Li, B.; Shi, P.; Yang, T.; Han, B. Short-Term Photovoltaic Power Prediction Based on a Digital Twin Model. *J. Mar. Sci. Eng.* **2024**, *12*, 1219. [CrossRef]
22. Wang, C.; Song, X.; Fu, Q.; Cui, L.; Chen, P. Design and Optimization of PV Power Supply System for Marine Buoys. *J. Mar. Sci. Eng.* **2023**, *11*, 1808. [CrossRef]
23. Margossian, C.C.; Hoffman, M.D.; Sountsov, P.; Riou-Durand, L.; Vehtari, A.; Gelman, A. Nested $\hat{R}$: Assessing the convergence of Markov chain Monte Carlo when running many short chains. *Bayesian Anal.* **2025**, *20*, 1587–1614. [CrossRef]
24. Yu, D.; Yang, J.; Shi, L.; Zhang, Q.; Huang, K.; Fang, Y.; Zha, Y. On the uncertainty of initial condition and initialization approaches in variably saturated flow modeling. *Hydrol. Earth Syst. Sci.* **2019**, *23*, 2897–2914. [CrossRef]
25. Wang, W.; Fu, Z.; Liang, X.; Yi, H.; Chen, L. Enhancing self-sustainability via robust speed optimization for an unmanned photovoltaics-battery vessel under solar irradiance and sea wave uncertainties. *Energy* **2026**, *342*, 139440. [CrossRef]
26. Fu, Z.; Chen, W.; Chen, L. Energy management strategy based on wave height and photovoltaic real-time prediction for pv-diesel-battery unmanned surface vessel. *J. Mech. Eng.* **2025**, *61*, 293–304. [CrossRef]
27. Yang, B.; Wang, Q.; Wang, C.; Chen, Z.; Huang, Y.; Gu, H. Evaluation and construction of index system of intelligent unmanned surface vessels. In Proceedings of the 2023 International Conference on Marine Equipment & Technology and Sustainable Development, Beijing, China, 1 April 2023; pp. 845–855.
28. Xiao, G.; Ren, B.; Tong, C.; Hong, X. A Quantitative Evaluation Method for Obstacle Avoidance Performance of Unmanned Ship. *J. Mar. Sci. Eng.* **2021**, *9*, 1127. [CrossRef]
29. Li, L.; Zhang, G.; Cao, B.; Wang, S.; Tian, Y. Dynamic adaptive weighting of effectiveness assessment indicators: Integrating G1, CRITIC and PIVW. *Comput. Mater. Contin.* **2026**, *86*, 1–26. [CrossRef]
30. Carrière, T.; Amaro e Silva, R.; Zhuang, F.; Saint-Drenan, Y.-M.; Blanc, P. A new approach for satellite-based probabilistic solar forecasting with cloud motion vectors. *Energies* **2021**, *14*, 4951. [CrossRef]

Disclaimer/Publisher's Note: The statements, opinions and data contained in all publications are solely those of the individual author(s) and contributor(s) and not of MDPI and/or the editor(s). MDPI and/or the editor(s) disclaim responsibility for any injury to people or property resulting from any ideas, methods, instructions or products referred to in the content.